Delft University of Technology

Gravity-Field Estimation of Asteroids

Mooij, E.; Root, B.C.

Important note
To cite this publication, please use the final published version (if applicable).
Please check the document version above.

Gravity-Field Estimation of Asteroids

Erwin Mooij* Bart Root† and Aurelia Bourgeaux ‡

Delft University of Technology, Faculty of Aerospace Engineering,

Kluyverweg 1, 2629 HS Delft, The Netherlands

With the increasing interest in the Solar System's smaller bodies, quite a few missions have been sent to comets and asteroids, and more will be send in the near future. Due to the large distances involved, communication to command mission parameters takes a long time, which has a negative impact on operational safety. Autonomous navigation would be one of the key technologies that can make the mission more robust, safe, and cost effective. This is especially true if one considers the unknown flight environment when the spacecraft is first encountering the body. Most asteroids and comets have a very irregular shape and unknown mass distribution. Therefore, knowledge about its irregular gravity field will be directly beneficial as input to orbital corrections and manoeuvre planning. This paper addresses the estimation process of gravity-field parameters that could potentially be implemented in an autonomous navigation system. The focus is on a spherical-harmonic modelling of asteroid Eros-433, most notably outside the Brillouin sphere where the validity of the model is guaranteed. By using Kalman filtering it is shown that all degree and order coefficients up to degree 8 can be estimated with an error below 10%. This is the first step towards an autonomous navigation system that can operate in a highly-perturbed environment close to the asteroid.

I.   Introduction

The small bodies in the Solar System, typically consisting of asteroids and comets, are seen as windows to the history of the Solar System and to different stages of planetary formation, what makes their exploration scientifically valuable. But also for more mundane reasons, these bodies are of interest. It is believed that in the future these bodies can provide minerals no longer available in abundance on Earth, which would make asteroid mining a commercially attractive business. And last but not least, the danger of an asteroid hitting Earth is not exactly zero, so finding ways to deflect asteroids is a relevant research area. Given these reasons, in the past several missions have been sent to asteroids and comets and more will follow in the near future.

One issue with such missions is that due to the distance from Earth, communication delays can be significant, and also mission operators on Earth have to rely on the data sent back from the spacecraft. To increase mission robustness and flight safety, it could be beneficial for the spacecraft to rely on autonomous navigation. Because the flight environment of asteroids and comets is not well known at first arrival – the shape may be known, but not the mass distribution and therefore the gravity field, which can be highly irregular – the flight control system will benefit of establishing a detailed and accurate model of the small-body's gravity field.

This paper aims at setting up a methodology to contribute to just that. Based on a detailed "real-world" simulator, orbits around a small body can be simulated that are perturbed by non-linear gravity effects, as well as solar-radiation pressure and third-body perturbations. After measuring, for instance, land marks on the small-body's surface that can be processed (in a preliminary mission phase with Earth in the loop), they can be combined into a detailed land-mark database, which can then be subsequently used to determine the (relative) position and velocity of the spacecraft with respect to the body [1]. A next step would then be to use measurements of orbital perturbations to estimate as many components of the body's gravity field

---

*Associate Professor, Section Astrodynamics and Space Missions, e.mooij@tudelft.nl. Associate Fellow AIAA.

†Assistant Professor, Section Planetary Exploration, b.c.root@tudelft.nl

‡MSc Student, Section Astrodynamics and Space Missions. Currently: Orbit determination and Navigation engineer, CNES, France, aurelia.bourgeaux@cnes.fr.

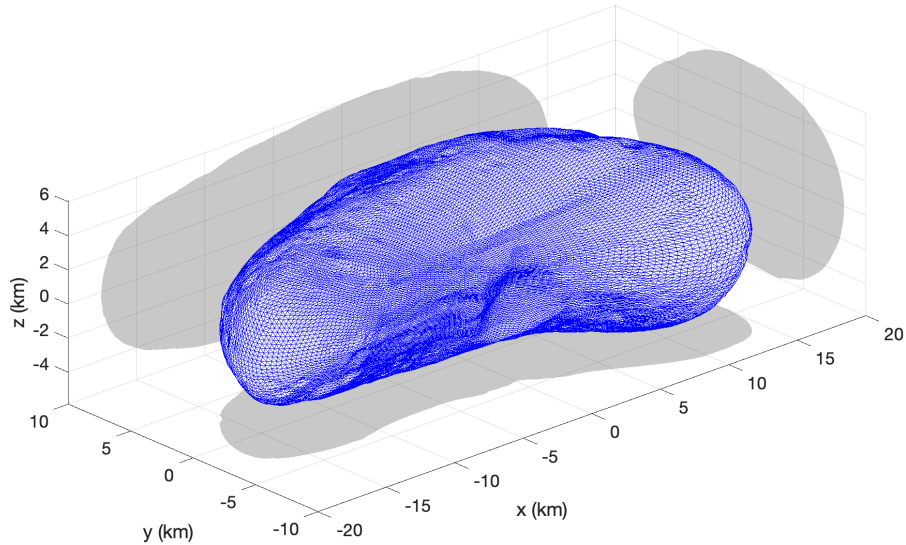American Institute of Aeronautics and Astronautics

Figure 1. High-resolution polyhedron model of Eros-433. Data source: see Footnote a.

as possible. Detailed knowledge about the gravity field can then be used for planning science and mission operations, such as orbital corrections.

The aim of the current paper is to set up a methodology that can serve as a development platform for autonomous navigation systems. Even while using simplified sensor models, a lot of insight can be gained and shortcomings in the modelling approach can be identified. To this end, the layout of the paper covering the proposed research is as follows. Section II describes the physics behind the simulation model, *i.e.,* the target asteroid Eros-433, and the spacecraft's flight dynamics. In the next Sec. III the simulation and estimation methodology is introduced, providing a brief description of the simulator used and the proposed navigation filters (extended and unscented Kalman filter). Then, Sec. IV presents some of the results of this study and indicates the logical next steps in the research. Section V concludes the paper with some final remarks.

II.   Model

Eros-433 is an elongated body, resembling an ellipsoid, with dimensions of 33 by 13 by 13 km (see Figure 1[a]), and rotates with an approximate constant rate in 5.27 hours (such that the rotational rate is $\boldsymbol{\omega}_{cb} = (0, 0, \omega_{cb,z})^{\mathrm{T}} = (0, 0, 3.3244 \cdot 10^{-4})^{\mathrm{T}}$ rad/s). Eros has been visited by the NEAR/Shoemaker spacecraft in 1998 that yielded a large amount of observational data from which the physical properties could be estimated [2, 3].

For the "real-world" asteroid model, a gravity field up to order and degree 16 has been determined, results of which are shown in Figure 2 for two different altitudes, *i.e.,* 25 km and 16 km. The results shown are the deviations from the point-mass model and thus highlighting the irregularities of Eros' gravity field. It also shows that with increasing altitude these irregularities are much more "smeared out" and will thus be harder – not to say *impossible* for some effects – to estimate. Additional effects taken into account for this "real world" are a constant rotational rate, the perturbing gravitational effect of the Sun, and solar-radiation pressure.

The equations of translational motion follow directly from Newton's second law:

$$\dot{\mathbf{v}} = \mathbf{a_g} + \mathbf{a_3} + \frac{\mathbf{F_{srp}}}{m} \qquad \text{and} \qquad \dot{\mathbf{r}} = \mathbf{v} \tag{1}$$

with $\mathbf{v}$ and $\mathbf{r}$ being the inertial Cartesian velocity and position, and $\mathbf{a}$ the external acceleration with subscripts *g* and *3* indicating the asteroid's gravity and the gravitational attraction of a third body, in this case the Sun. The acceleration due to solar-radiation pressure (subscript "srp") can be derived from the pressure

---

[a]Data are taken from the small-body catalogue, in particular the NEAR collected shape and gravity models: https://sbn.psi.edu/pds/resource/nearbrowse.html, date accessed May 15, 2022.

American Institute of Aeronautics and Astronautics
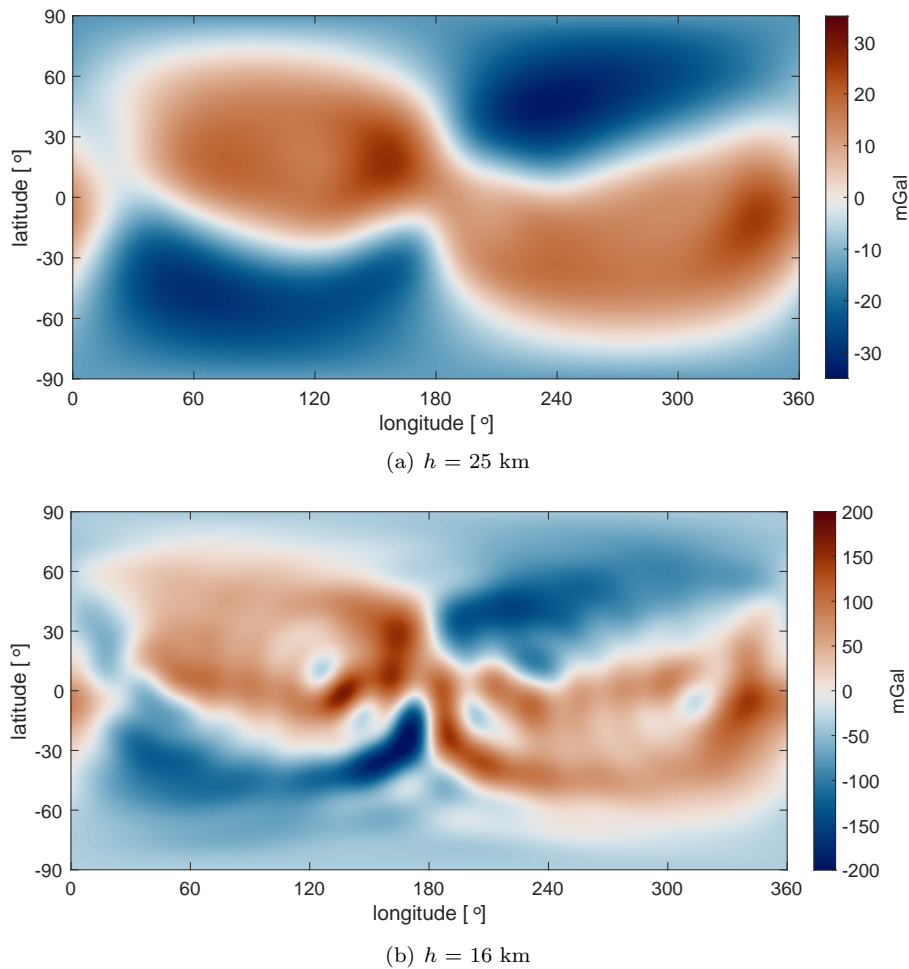
(a) $h = 25$ km

(b) $h = 16$ km

Figure 2. Gravitational anomalies with respect to the point-mass gravity at 25 km (top) and 16 km (bottom) altitude above the centre-of-mass location, for a complete range of longitude and latitude.

force acting on the exposed walls of the satellite divided by the satellite's mass, m. Note that the motion is expressed in the inertial frame, $\mathcal{F}_i$.

The gravity field of the asteroid can be represented in different ways. For the elongated shape of Eros, a so-called polyhedra model would be best, as it can define gravity for any orbital altitude down to the surface. However, it requires a significant CPU load and the resulting field is not easily identified with noticeable parameters. An alternative is to use spherical harmonics, which has as a restriction that it can only be used for more or less spherical bodies. In case of elongated bodies, the limit distance is defined by the Brillouin sphere, an encapsulating sphere with a radius defined by the body's largest dimension. Despite this disadvantage, in case of Eros the orbital altitude cannot be lower than 16 km, the model has identifiable coefficients that could potentially be estimated by the navigation filter. For this reason, and to keep the methodology simple and understandable, the spherical-harmonic model is chosen.

The gravity acceleration, $\mathbf{g_v}$, is expressed in the local north-east-down or *vertical* frame, $\mathcal{F}_v$, as [4]:

$$\mathbf{g_v} = \begin{pmatrix} g_n & g_e & g_d \end{pmatrix}^{\mathrm{T}} = \begin{pmatrix} -\frac{1}{r}\frac{\partial U}{\partial \delta} & -\frac{1}{r\cos\delta}\frac{\partial U}{\partial \tau} & -\frac{\partial U}{\partial r} \end{pmatrix}^{\mathrm{T}} \tag{2}$$

where the relative position with respect to the body is defined in spherical coordinates, *i.e.*, r is the distance between the spacecraft and the body's centre of mass, and τ and δ are longitude and latitude, respectively, which relate $\mathcal{F}_v$ to the rotating, asteroid-fixed frame, $\mathcal{F}_r$. It is assumed that $\mathcal{F}_r$ and $\mathcal{F}_i$ are collinear at $t = 0$. This implies that τ is expressed with respect to the zero meridian, defined by the $x_r z_r$-plane, and δ with respect to the mean equatorial plane, defined by $x_r y_r$. Longitude and latitude can be obtained from the inertial position, $\mathbf{r} = (x_i, y_i, z_i)^{\mathrm{T}}$ in two successive steps:

American Institute of Aeronautics and Astronautics

$$x_r = \cos(\omega_{cb,z}t)x_i + \sin(\omega_{cb,z}t)y_i \qquad y_r = \sin(\omega_{cb,z}t)x_i + \cos(\omega_{cb,z}t)y_i \qquad z_r = z_i \qquad (3)$$

which gives the Cartesian position in $\mathcal{F}_r$, and then:

$$r = \sqrt{x_r^2 + y_r^2 + z_r^2} \qquad \tau = \arctan\left(\frac{y_r}{x_r}\right) \qquad \delta = \arcsin\left(\frac{z_r}{r}\right) \qquad (4)$$

In Eq. (2), U is the so-called gravitational potential, formulated as a spherical-harmonics expansion:

$$U = \frac{\mu}{R}\left\{\sum_{n=0}^{\infty}\sum_{m=0}^{n}\left(\frac{R}{r}\right)^{n+1}\bar{P}_{nm}(\sin\delta)[\bar{C}_{nm}\cos(m\tau) + \bar{S}_{nm}\sin(m\tau)]\right\} \qquad (5)$$

with $\mu = GM$ being the gravitational parameter and R the reference radius of the asteroid, defining the Brillouin sphere below which the model is no longer valid. The fully-normalised associated Legendre polynomials of the first kind are represented by $\bar{P}_{nm}$, and the corresponding coefficients are given by $\bar{C}_{nm}$ and $\bar{S}_{nm}$. It is these latter two sets of coefficients that are added to the state vector with the three-dimensional position and velocity, $\mathbf{r}$ and $\mathbf{v}$. Of course, the degree and order of these coefficients cannot be infinitely large. Amongst others, observability of the maximum degree and order will be output of this study. To have a consistent dataset, and to be able to use a higher degree and order than which is available from observation data, the approach as discussed in Ref. [5] has been used to determine $\bar{C}_{nm}$ and $\bar{S}_{nm}$. With an average asteroid density of 2.621 g/cm^3, this yields a gravity acceleration at the surface of about 0.0059 m/s^2.

Since the gravitational acceleration is defined in $\mathcal{F}_v$, $\mathbf{g_v}$ has to be transformed to $\mathcal{F}_i$:

$$\mathbf{g_i} = \mathbf{C_{i,v}}\mathbf{g_v} \qquad (6)$$

with $\mathbf{C_{i,v}}$ being the transformation matrix from $\mathcal{F}_v$ to $\mathcal{F}_i$. This matrix can be obtained from individual unit-axis transformations, *i.e.*, $\mathbf{C_{i,v}} = \mathbf{C_z}(-\omega_{cb,z}t)\mathbf{C_z}(-\tau)\mathbf{C_y}(\pi/2 + \delta)$. The notation $\mathbf{C_i}(\alpha)$ indicates a rotation about axis i over an angle α.

To conclude the model description, instead of applying the coordinate transformation given by Eqs. (3) and (4), and an equivalent transformation for the velocity[b], the satellite's motion can also be directly solved in the rotating asteroid frame. This formulation will be the basis for the unscented Kalman filter, to be discussed later. The corresponding equations of motion are given by:

$$\dot{\mathbf{v}}_\mathbf{r} = \frac{\mathbf{F_r}}{m} - 2\boldsymbol{\omega}^\mathbf{r}_\mathbf{r/i} \times \mathbf{v_r} - \boldsymbol{\omega}^\mathbf{r}_\mathbf{r/i} \times (\boldsymbol{\omega}^\mathbf{r}_\mathbf{r/i} \times \mathbf{r_r}) \qquad (8)$$

$$\dot{\mathbf{r}}_\mathbf{r} = \mathbf{v_r} \qquad (9)$$

with $\boldsymbol{\omega}^\mathbf{r}_\mathbf{r/i} = \boldsymbol{\omega}_\mathbf{cb}$ being the rotation of $\mathcal{F}_r$ with respect to $\mathcal{F}_i$, expressed in components of $\mathcal{F}_r$, and

$$\frac{\mathbf{F_r}}{m} = \mathbf{g_r} = \mathbf{C_{r,v}}\mathbf{g_v} \qquad (10)$$

In future research, when thrusted manoeuvres may be studied for orbital corrections, $\mathbf{F_r}$ will include a propulsive component as well.

III.   Methodology

The methodology that has been setup is the following. A simulator has been developed that allows for simulating different types of orbits around small bodies. The underlying models are:

1. The flight dynamics includes translational motion based on Newton's equations of motion. Rotational dynamics can easily be added, but for now it has been excluded

---

[b]This transformation is defined to be

$$\mathbf{v_r} = \mathbf{C_{r,i}}(\mathbf{v_i} - \boldsymbol{\omega}_\mathbf{cb} \times \mathbf{r_i}) \qquad (7)$$

American Institute of Aeronautics and Astronautics

2. The flight environment is centred around a rotating small body, which, in the current study, is asteroid Eros-433. The asteroid rotates with a constant angular rate, although this is, strictly speaking, not a requirement. Its gravity field is defined as a spherical-harmonic model of degree and order 22 for a complete simulation. If needed, a lower degree and order can be selected by the user. An alternative polyhedra model has been implemented for verification purposes, and to allow for future studies of proximity operations.

3. Perturbing accelerations originate from solar-radiation pressure and third bodies (currently the Sun only), and, depending on the simulation mode, they can either be switched on or off.

4. Part of the navigation system are simplified sensors, which provide noisy position and/or velocity measurements in either $\mathcal{F}_i$ or $\mathcal{F}_r$, depending on the filter implementation. Interfacing with more realistic sensors is possible, but is left as future extension.

5. The core of the navigation system is an augmented state estimator, based on the well-known Kalman filter. Two variations will be studied: the industry-standard extended Kalman filter (EKF) and the unscented Kalman filter (UKF). The latter was found to be more robust and converge faster in some applications, but at the expense of a larger computational load [6]. The mathematical foundation of both EKF and UKF can easily be found in literature, but has been provided in the appendix for the reader's benefit.

Before the spacecraft is in close proximity of the asteroid, a visual inspection of the asteroid at a higher (stable) orbit may take place. Data are sent back to Earth and combined with possible ground-based observations. From these data a preliminary shape model can be constructed, defining the dimensions of the asteroid, and from sequential images the asteroid's angular rate can be derived. Thus, as a starting point of the research, it is assumed that both R and $\boldsymbol{\omega}_{cb}$ are known. These two parameters can directly be used in combination with Eq. (5), the gravitational potential, and Eq. (8), the dynamics system describing the motion with respect to a rotating asteroid.

The successive steps that are taken in the research can be divided over three categories. In the first category the effect of solar-radiation pressure and the gravitational attraction of the Sun on the estimation of the gravitational parameter, μ, of Eros will be studied. If the effect is found to be large, the conclusion to be derived could be to estimate these perturbations first before moving closer to Eros to estimate gravity-field parameters. The second category focusses on determining which filter is better suited for this research, *i.e.,* the EKF or UKF. Following the outcome of that, the "best" filter will be used for the simulations in the third category, *i.e.,* the estimation of the gravity-field coefficients $\bar{C}_{nm}$ and $\bar{S}_{nm}$.

IV. Results

A. Perturbing Accelerations

Initial runs show that the effect of the gravitational attraction of the Sun and solar-radiation pressure are large, and even dominating outside the sphere of influence of the asteroid. The Sun is at a distance of $s_\odot$ = 218.155·10^6 km from Eros, which defines the radius of the sphere of influence to be R_{SoI} = 366.437 km. Two sets of simulations show what the effect of the third-body perturbation is on the estimated value of the gravitational parameter, μ[c]. Six runs per set are executed, assuming a circular orbit with radii of 150, 250, 350, 500, 1,000, and 1,500 km. For now, the EKF is used with noisy position measurements as input (σ_r = 10 m, Gaussian white noise), at a frequency of 1 Hz. It should be mentioned that any hardware performance of the on-board computer is currently not considered. This is left as future work.

The state-estimation results are shown in Figure 3(a). While being close to Eros, the estimates are decent enough, but while getting close to R_{SoI}, the estimation errors in μ are increasing. Beyond R_{SoI}, the unmodelled third-body attractions are too large to make the estimation process reliable. The approach should thus be that the effect of the third-body attraction of the Sun is estimated first, while still being far away from Eros. Once achieved, a correction term can be added to the filter model. Of course, a decent theoretical initial guess exists, so this should be easily achieved. With this correction now implemented in the filter and running the simulations again for the same orbital radii, gives the results shown in Figure 3(b).

---

[c]In parallel, also $\bar{C}_{2,0}$ is estimated, but in the presence of the large perturbation this is not successful.
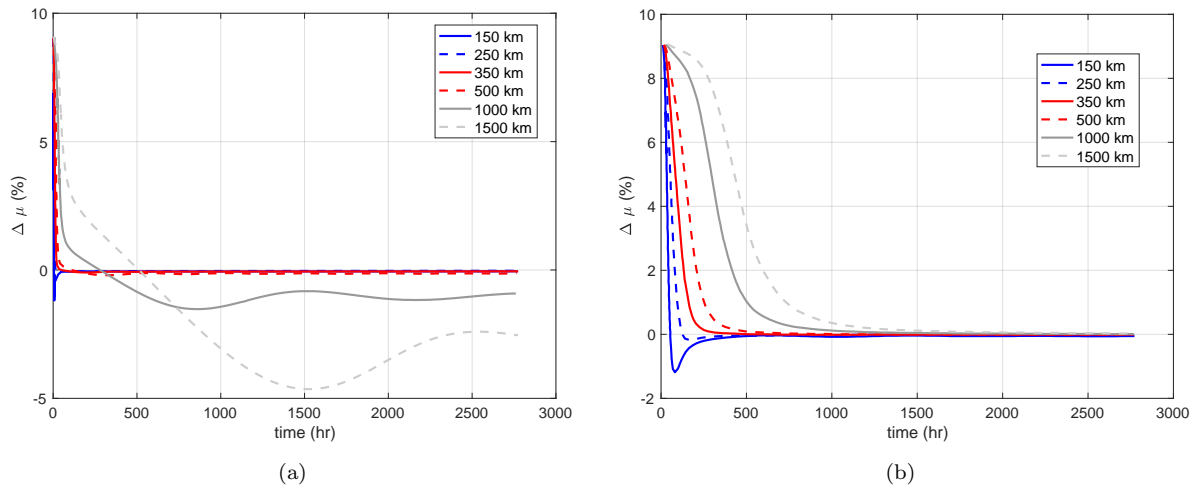
Figure 3. Relative estimation error in μ as a function of time in the presence of the Sun as third body. Left: $\mathbf{a_3}$ is a perturbing acceleration, right: $\mathbf{a_3}$ is assumed estimated.

A distinct improvement is observed, which was to be expected[d]. The effect that remains is that at larger distances the gravitational pull of Eros is weaker, which results in a slower convergence of the EKF.

The next effect to be studied is that of the solar-radiation pressure, hereby assuming that the third-body perturbation will be corrected for in the filter. In the vicinity of Eros, the solar flux is $\Phi = 622$ W/m^2, resulting is a radiation pressure of $p_{srp} = 2.073 \cdot 10^{-7}$ N/m^2. The current implementation to calculate $\mathbf{a_{srp}}$ is that the satellite is modelled as a canon ball, with a reference area of 2 m^2 and a reflection coefficient of C_r = 1. The satellite mass is $m = 1,000$ kg. The same orbital altitudes ranging from 1500 down to 150 km were chosen, and the estimation process was repeated with and without the solar-radiation pressure included.

Figure 4(a) shows the relative estimation error when $\mathbf{a_{srp}}$ is simply an unmodelled perturbing acceleration. A similar effect as with $\mathbf{a_3}$ can be observed. In the highest orbit the filter is slowly diverging, which may indicate a retuning of the filter is required. However, since the conclusion is obvious, this is not done; instead, a correction term is added to the filter. Figure 4(b) shows the convergence plot for estimating μ, when solar-radiation pressure is included. The remaining error is well below 0.1% for the different altitude; obviously, this is the same result as shown in Figure 3(b), but the graph is included for easy comparison.

B. Filter Trade-off

In this section, the performance of both EKF and UKF is compared. In all fairness, the choice to continue with the UKF was already made for a different reason, but the comparison serves as a verification test that the UKF is correctly implemented[e]. Despite being a more complex filter, because of the increased number of tuning parameters and the additional implementation of the sigma points that make the filter slower in execution, there is a principal advantage of the UKF over the EKF. With increasing augmented state vector, the dimensions of the Jacobians (in particular the state-transition matrix) grow rapidly. In case one wants to use analytical derivatives, setting up these matrices is a tedious task. The UKF does not share that problem, as no Jacobians are required. It is therefore a lot easier to simply expand the dynamics model of the filter.

Nonetheless, the current test will be executed for the case of a central gravity field, where the filters have to estimate μ besides velocity and position. No further perturbations are modelled. The dynamics model of the EKF is based on Eq. (1), whereas that of the UKF uses Eqs. (8) and (9). A passed verification test would not just confirm a proper filter implementation, but also the correct implementation of the equations

---

[d]In the current, preliminary research, the perturbing accelerations are studied in an isolated manner, *i.e.,* the third-body perturbation is assumed to be the only one, without solar-radiation being present. In the next batch, the situation is reversed, when only the solar-radiation pressure is included. Once the filter designs have converged, an integrated analysis should confirm the stepwise approach, with all perturbations acting at the same time. This detailed analysis, no matter how critical for proof of concept, remains to be done.

[e]The implementation of the EKF is a lot simpler and more straightforward. Also, many examples exist in literature that can serve as verification tests of the EKF. Therefore, the EKF provides a solid basis as a benchmark filter.
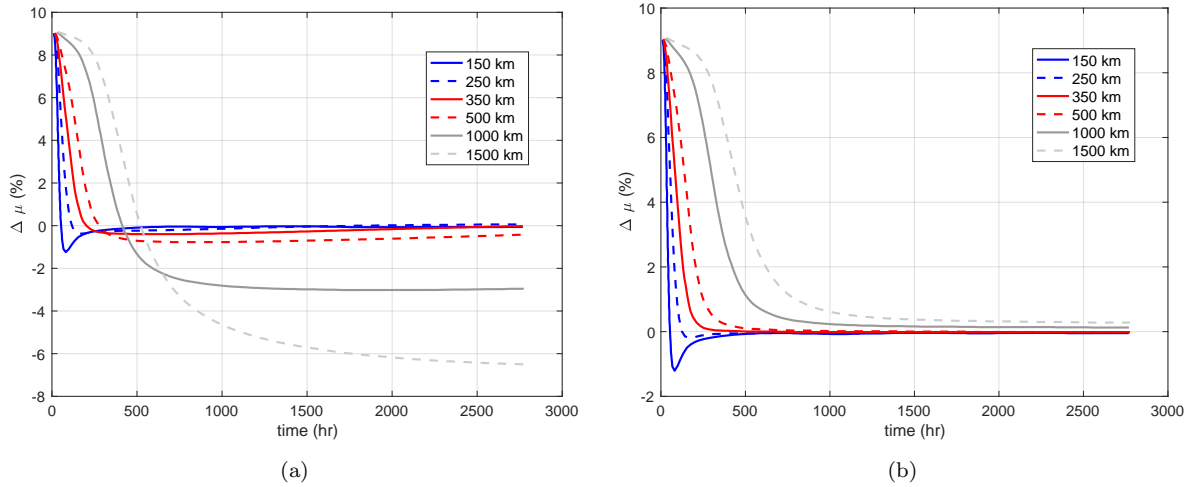
American Institute of Aeronautics and Astronautics

Figure 4. Relative estimation error in μ as a function of time in the presence of solar-radiation pressure. Left: $\mathbf{a_{srp}}$ is a perturbing acceleration, right: $\mathbf{a_{srp}}$ is assumed to have been estimated.

of motion.

The mission to be simulated is a circular, equatorial orbit with a radius of 100 km, where the circular velocity is about 2.1 m/s. Nonetheless, the initial estimation errors are 1 m/s for each Cartesian velocity component, whereas the position errors are 100 m, 0.1, and -1 m in x, y, and z, respectively. The initial error in μ is 1,350 m^3/s^2. Ccompared to the nominal value of $\mu = 440{,}135.0$ m^3/s^2 this is only an error of about 0.31%. However, it was observed that the filter had some difficulties estimating μ, because of the relatively large velocity and x-position errors. This would induce a much larger error into the filter. The external measurements are noisy position coordinates, *i.e.,* the actual values with a white-noise component with a standard deviation of 10 m added to it. It is assumed that this level of accuracy can be achieved with current sensors, but later in this section it will be shown what the effect of larger noise values on the estimation process will be.

Figure 5 shows the results of the two simulations, one with the EKF as the estimator and one with the UKF. Early on in the estimation process, μ is not estimated correctly; the effect of large initial errors in $\mathbf{v}$ and x is clearly noticeable. However, after a few thousands of seconds the filter converges rapidly, for each of the seven states (velocity, position, and μ). Since both filters behave in a similar fashion, with two principally different underlying models, the verification of the UKF is successful. Another equally important conclusion can be drawn, while comparing the results. The UKF converges quicker than the EKF (it also has a tighter bound on the error covariance), and the final estimation error after 45,000 s ($\approx$ 2.4 orbits) is smaller as well. Combined with the ease with which the UKF's augmented state vector can be extended, the UKF is the filter of choice for this research.

C.   Higher-Order Coefficients

The last part of the research focusses on the estimation of higher-order coefficients. The foreseen approach is as follows. At large distance, when Eros can almost be considered to be a mass point, even though the complete spherical-harmonics model is simulated as the "real world", the navigation filter will begin its process with estimating μ, and possibly $\bar{C}_{2,0}$ (as $\bar{S}_{2,0}$ does not exist). If Eros is far enough, the non-linear perturbations in gravitational acceleration are minimal, and an accurate estimate of μ can be obtained. Therefore, in subsequent runs at lower altitudes, μ is "hardcoded" (= known) in the filter, in a similar way as $\mathbf{a_3}$ and $\mathbf{a_{srp}}$. When in addition only $\bar{C}_{2,0}$ is being estimated (not shown here), it was found to converge best at an altitude of 45 km: at higher altitudes the $\bar{C}_{2,0}$ effect starts to decrease and becomes less noticeable, whereas at lower altitudes the effect of the higher-order terms start dominating. The remaining error is about 6%. This could be an alternate approach, though: first estimate μ and then $\bar{C}_{2,0}$, after which both are taken as known values in the filter. However, for now only μ is assumed to be known, and the focus will be on estimating all higher-order coefficients as well.

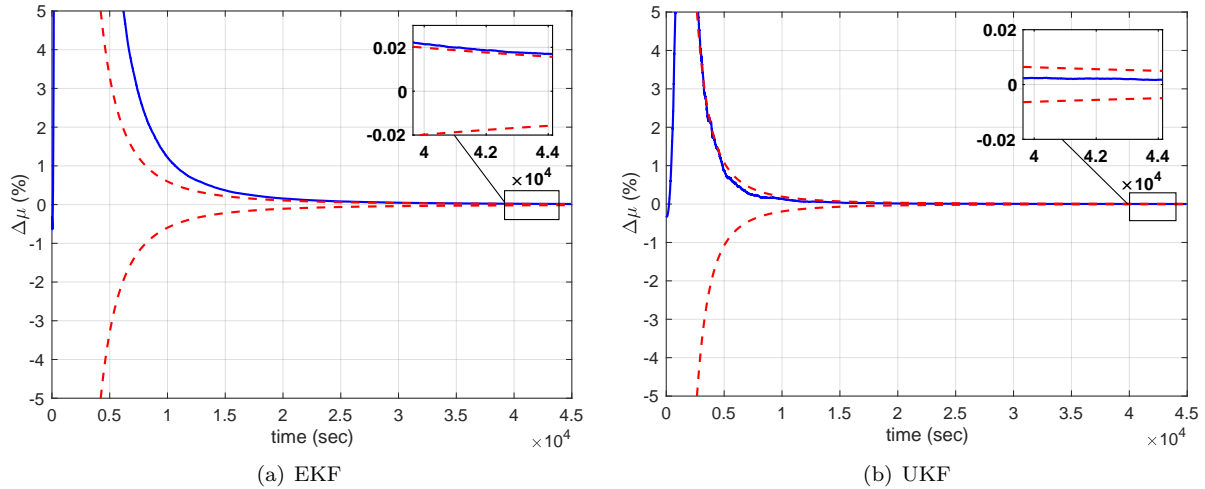American Institute of Aeronautics and Astronautics

Figure 5. Estimation of μ, comparison of filter performance. Equatorial orbit with radius of 100 km.

At the same time, the effect of noise in the external measurements on the estimation process is considered. A range of coefficients of up to degree 8 will be estimated with position measurement-noise of σ_p, is 1,000 m, 100m, and 10 m. For this particular simulation, the spacecraft is orbiting Eros in a circular polar orbit at an altitude of 45 km. The results of the estimation are shown in Figure 6, where the final estimation error is shown for all estimated coefficients. In this figure, the negative-order coefficients represent the S_{ij} coefficients, whereas the positive values represent the C_{ij} coefficients. These results indicate that lower noise values on the measurements reduce the estimation errors, such that higher degree-and-order coefficients at 45 km altitude can be determined. This could be explained by the fact that the small changes in the dynamics due to the high spherical harmonic values are hidden by large noise on the position measurements. Therefore, the measurement noise should be as low as possible, such that the coefficients of high degree and order are more noticeable in the system dynamics for optimal estimation. We can also see that with $\sigma_p = 10$ m, it is possible to estimate all coefficients up to degree 8. Of course, future research should be aimed at developing more realistic sensor models to be included in the simulator.

Two more cases are evaluated, one with an orbital altitude of $h = 50$ km and another one with $h = 35$ km, with the noise level on the position measurements set to the low value of 10 m. Figure 7(a) displays the errors of the full 8 degree and order coefficients of the gravitational field of Eros for the estimation at an orbital height of 50 km. The coefficients of degree 6 and higher have significant errors, but the coefficients up to degree and order 5 can be estimated within errors of less than 30%. The estimation accuracy significantly improves, when the orbit is lowered to 35 km and the measurement time is extended to 10 days. Figure 7(b) shows that all coefficients up to degree and order 8 can be estimated with average errors of about 10% (with maximum outliers at about 20%). These results are promising enough to warrant further study with realistic sensor models, and more detailed and varied mission scenarios.

Of course, while estimating the gravity-field coefficients also velocity and position have been estimated, as in an actual mission design they would be a direct input to the orbit control system (not modelled here). The resulting estimates are shown in Figure 8. It is clear that the remaining errors are very small. However, this is mainly attributed to the relatively ideal measurements.

V.   Concluding Remarks

A step-wise exploration mission to estimate the gravitational perturbations of an irregular body, like the Eros asteroid, is feasible with an unscented Kalman filter (UKF). Several steps should be executed in order to do so, the first being to estimate the effect of third-body perturbation of the Sun, as well as the solar-radiation pressure, while still being outside the sphere of influence of the asteroid. The next step is to characterise the shape and rotational rate of the asteroid, such that a reference radius for the spheric-harmonic gravity field is available, as well as the option to use a dynamics model defined in the asteroid-fixed
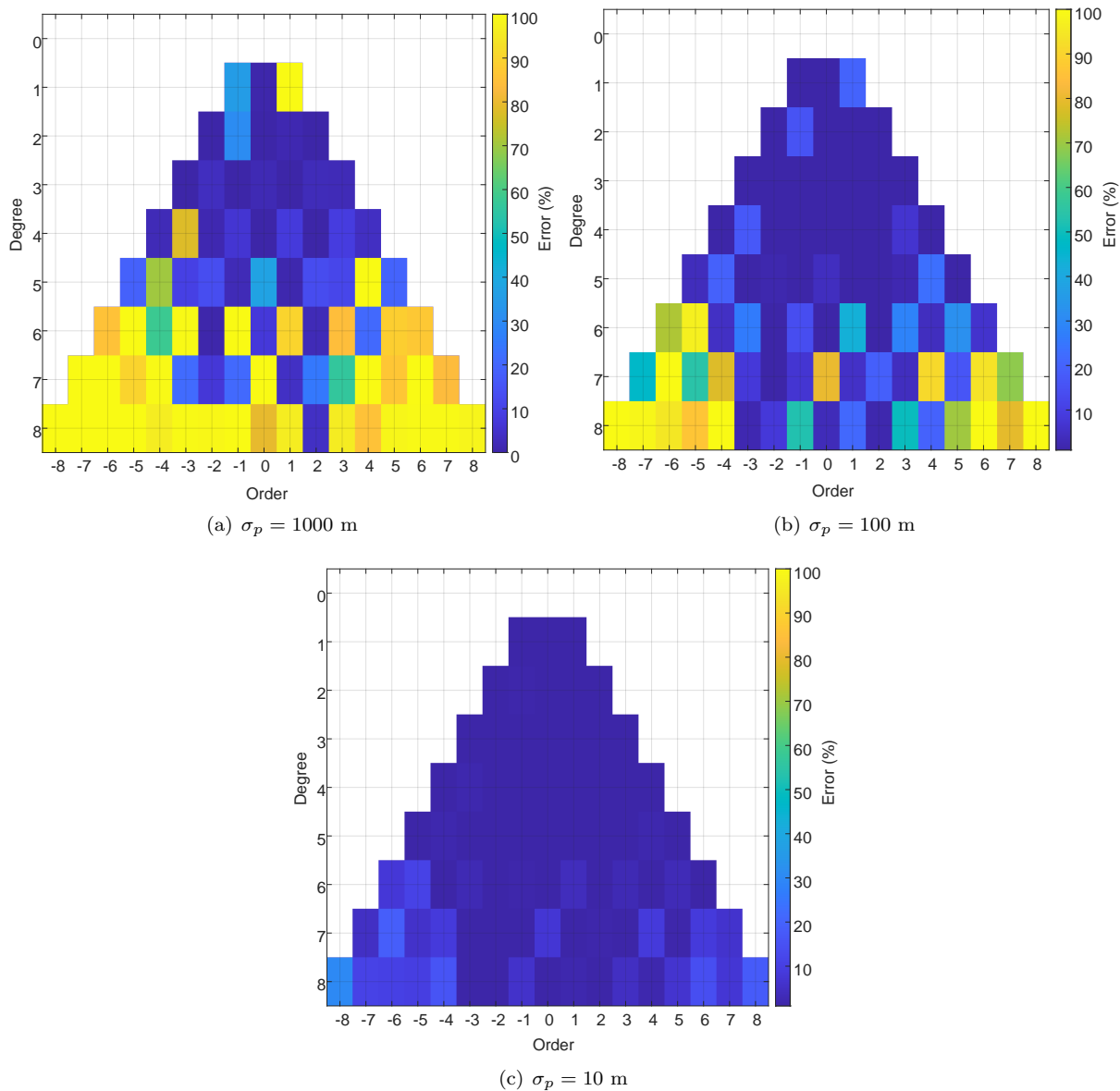
(a) $\sigma_p = 1000$ m

(b) $\sigma_p = 100$ m

(c) $\sigma_p = 10$ m

Figure 6. Coefficient-estimation errors as a function of position-measurement noise, σ_p. Orbital radius 45 km.

frame in the UKF.

Then, a decrease of orbital altitude to go into the sphere of influence is envisioned to estimate the central-field gravity parameter, μ, and possibly the $\bar{C}_{2,0}$. The solar radiation pressure and third body forces need to be modelled with sufficient accuracy. The third step is followed by updating the UKF with the estimated μ and $\bar{C}_{2,0}$ values, before flying to a close proximity orbit and estimating higher order and degree coefficients.

Simulations show that at an altitude of 35 km with a position error of several meters, up to order and degree 8 can be estimated within a few days. The UKF is able to perform these calculations in real-time and could therefore be included in the autonomous guidance, navigation, and control (GNC) system of the satellite.

Future work envisions to fly lower and explore different mathematical representations of the gravity field to even fly lower than the Brillioun sphere. Techniques based on, for instance, mascon models or even physics-informed neural networks, will allow the GNC system to become more autonomous. Moreover, a multitude of realistic sensor and instrument models for the navigation data should be evaluated, to converge to the optimal sensor suit. In this context, real-life sensor-error behaviour can be be studied in a dedicated
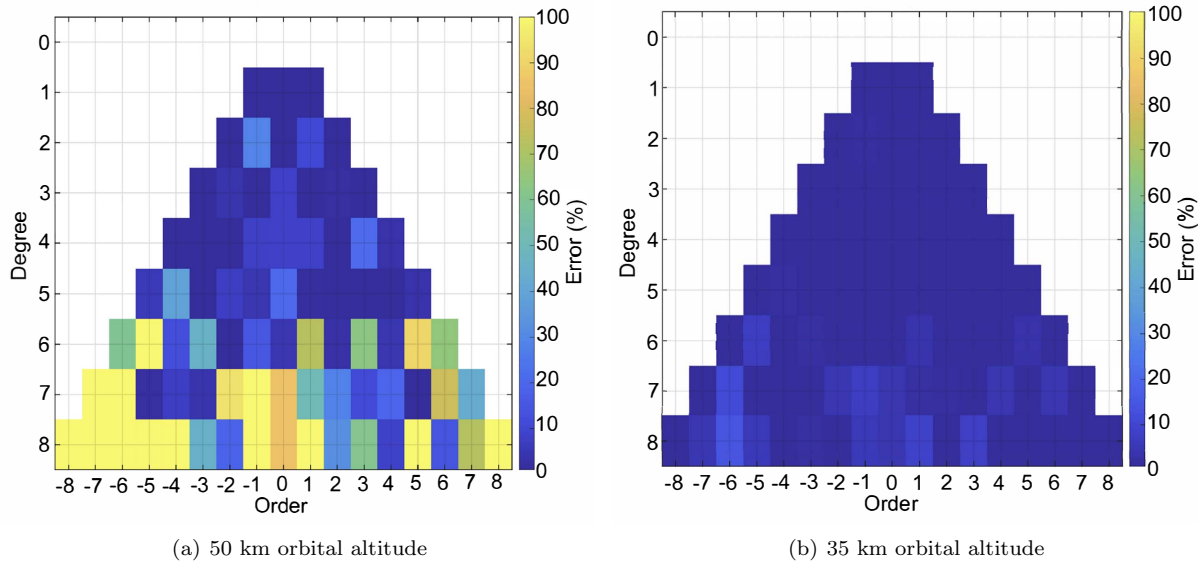
American Institute of Aeronautics and Astronautics

(a) 50 km orbital altitude

(b) 35 km orbital altitude

Figure 7. Estimation error for the spherical-harmonics coefficients at two orbital altitudes.
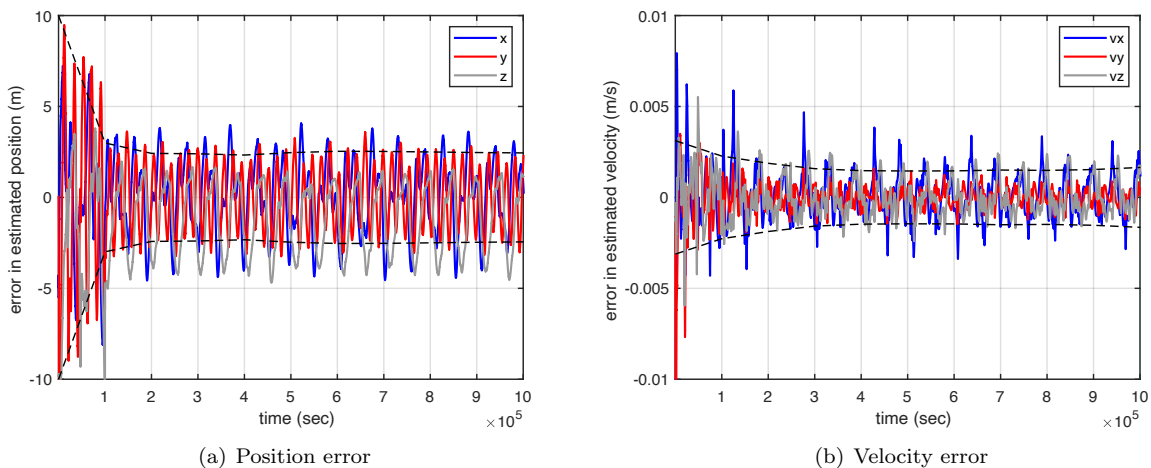

(a) Position error

(b) Velocity error

Figure 8. Estimation error for the position and velocity in a 35 km orbit.

GNC laboratory with different lighting conditions and high-resolution, 3D-printed asteroids. This allows for verification and validation of the simulation models, which will lead to more realistic simulation results. Each of these steps will lead to a better understanding of the optimal design for an autonomous GNC system to explore unknown asteroids.

Appendix - Estimation Filters

This appendix will summarise the two filters used in this study, *i.e.,* the extended Kalman filter (EKF), and the unscented Kalman filter (UKF).

A. Extended Kalman Filter

The EKF works by using a first-order Taylor series approximation of the non-linear system around the current estimate. The derivation of the EKF can be found in many textbooks, *e.g.,* [7], [8] and [9]. The

current description provides a summary of this derivation. The non-linear system may be expressed by the following discretised equation

$$\mathbf{x}_k = f\left(\mathbf{x}_{k-1}, \mathbf{u}_{k-1}\right) + \mathbf{v}_{k-1} \tag{11}$$

with the measurement

$$\mathbf{z}_k = h(\mathbf{x}_k) + \mathbf{w}_{k-1} \tag{12}$$

In these equations, $\mathbf{x}$ and $\mathbf{u}$ are the state and input vectors, respectively. The subscript k indicates the time stamp, t_k, with $k-1$ being the previous one. The noise parameters $\mathbf{v}_{k-1}$ and $\mathbf{w}_{k-1}$ are taken from a normal distribution,

$$\mathrm{p}(\mathbf{v}_k) \sim N(0, \mathbf{Q}_k) \qquad \text{and} \qquad \mathrm{p}(\mathbf{w}_k) \sim N(0, \mathbf{R}_k) \tag{13}$$

where the covariance matrices $\mathbf{Q}$ and $\mathbf{R}$ are tuning parameters (read: user input) in the filter-design process: the expected process and measurement noise, respectively.

The filter is then divided into two parts, *i.e.,* prediction and correction. In the prediction step, the so-called *a-priori* estimate is computed. Equation (11) can be used to compute the predicted state from the previous estimate, whereas Eq. (12) can be used to compute the predicted measurement from the predicted state. However, f and h cannot be applied to the covariance directly, and for that reason at each time step, the Jacobians are evaluated with current predicted states. Linearising Eqs. (11) and (12) yields:

$$\mathbf{F}_k = \left.\frac{\partial f}{\partial \mathbf{x}}\right|_{\hat{\mathbf{x}}_{k-1|k-1}, \mathbf{u}_k} \qquad \text{and} \qquad \mathbf{H}_k = \left.\frac{\partial h}{\partial \mathbf{x}}\right|_{\hat{\mathbf{x}}_{k|k-1}} \tag{14}$$

where $\mathbf{F}_k$ and $\mathbf{H}_k$ are the state transition and observation matrices, respectively. The notation $\hat{\mathbf{x}}_{n|m}$ represents the estimate of $\mathbf{x}$ at time n using all observations up to and including at time $m \leq n$.

The *a-priori* state estimate can be derived from the previous *a-posteriori* estimate using

$$\hat{\mathbf{x}}_{k|k-1} = f\left(\hat{\mathbf{x}}_{k-1|k-1}, \mathbf{u}_{k-1}\right) \tag{15}$$

whereas the associated error covariance can be predicted with

$$\mathbf{P}_{k|k-1} = \mathbf{F}_k \mathbf{P}_{k-1} \mathbf{F}_k^{\mathrm{T}} + \mathbf{Q}_{k-1} \tag{16}$$

In the correction step, first the innovation or measurement residual (the difference between the actual measurement and the predicted measurement) is calculated:

$$\mathbf{e}_{z,k} = \mathbf{z}_k - h(\hat{\mathbf{x}}_{k|k-1}) \tag{17}$$

Similarly, the innovation covariance is determined with

$$\mathbf{E}_{p,k} = \mathbf{H}_k \mathbf{P}_{k|k-1} \mathbf{H}_k^{\mathrm{T}} + \mathbf{R}_k \tag{18}$$

which is subsequently used to calculate the Kalman gain, $\mathbf{K}_k$:

$$\mathbf{K}_k = \mathbf{P}_{k|k-1} \mathbf{H}_k^{\mathrm{T}} \mathbf{E}_{p,k}^{-1} \tag{19}$$

Finally, the updated state and covariance updates follow from

$$\hat{\mathbf{x}}_{k|k} = \hat{\mathbf{x}}_{k|k-1} + \mathbf{K}_k \mathbf{e}_{z,k} \tag{20}$$

$$\mathbf{P}_{k|k} = \left(\mathbf{I} - \mathbf{K}_k \mathbf{H}_k\right) \mathbf{P}_{k|k-1} \tag{21}$$

American Institute of Aeronautics and Astronautics

B.   Unscented Kalman Filter

The state estimation principle of the UKF is similar to that of the EKF, in the sense that it applies an *a-priori* state and covariance estimate obtained through propagation of a system model that includes as much information about the dynamics as possible. Starting point is the model described by Eqs. (11) and (12). Principle difference with the EKF is that the state and covariance estimates are propagated through the propagation of a deterministically selected cloud of weighted points around the mean, the so-called sigma points, using the state equation Eq. (11). The sigma points are selected through the use of the unscented transform, which is a method to calculate the statistics of a random variable undergoing a nonlinear transformation [10]. The $2L + 1$ sigma-point vectors, where L represents the number of states in $\mathbf{x}$, can be calculated with:

$$\boldsymbol{\chi}_{0,k} = \hat{\mathbf{x}}_{k-1|k-1} \tag{22}$$

$$\boldsymbol{\chi}_{i,k} = \hat{\mathbf{x}}_{k-1|k-1} + \left(\sqrt{(L+\lambda)} \sqrt{\hat{\mathbf{P}}_{x_i}} \right) \qquad \text{for } i = 1, ..., L \tag{23}$$

$$\boldsymbol{\chi}_{i,k} = \hat{\mathbf{x}}_{k-1|k-1} - \left(\sqrt{(L+\lambda)} \sqrt{\hat{\mathbf{P}}_{x_{i-L}}} \right) \qquad \text{for } i = L, ..., 2L \tag{24}$$

where $\hat{\mathbf{P}} = \mathbf{P}_{k-1|k-1}$. Furthermore, the sigma-point vectors $\boldsymbol{\chi}_i^k$ are calculated using the current best estimate of state vector mean, $\hat{\mathbf{x}}_{k-1|k-1}$, and the ith row of the matrix square root of the current best estimate for the state covariance matrix, $\sqrt{\hat{\mathbf{P}}_{x_i}}$. With these sigma-point vectors, an $L \times (2L + 1)$ matrix $\mathbf{X}$ can be formed with corresponding weight factors, W_i^m and W_i^c:

$$W_0^m = \frac{\lambda}{L + \lambda} \tag{25}$$

$$W_0^c = \frac{\lambda}{L + \lambda} + \left(1 - \alpha^2 + \beta \right) \tag{26}$$

$$W_i^m = W_i^c = \frac{1}{2(L+\lambda)} \qquad \text{for } i = 1, ..., 2L \tag{27}$$

where λ is a scaling parameter: $\lambda = \alpha^2(L + \kappa) - L$. The parameter α determines the spread of the sigma points around the mean and is usually set to a small value, $\mathcal{O}\left(10^{-3}\right)$, κ is a secondary scaling parameter that is generally set to 0, and β is a parameter used to include knowledge on the distribution of the to-be-estimated parameter $\mathbf{x}$. For Gaussian distributions, an optimal value for β is 2.

With the sigma-point vectors established, a propagation through the nonlinear system dynamics can be performed to obtain an estimate of the sigma-point vectors at the next epoch:

$$\mathbf{X}_{i,k} = f(\boldsymbol{\chi}_{i,k-1}, \mathbf{u}_{k-1}) \qquad \text{for } i = 0, ..., 2L \tag{28}$$

Using this, an *a-priori* mean and state covariance matrix estimate follows from

$$\hat{\mathbf{x}}_{k|k-1} = \sum_{i=0}^{2L} (W_i^m \mathbf{X}_{i,k}) \tag{29}$$

$$\mathbf{P}_{k|k-1} = \sum_{i=0}^{2L} W_i^c \left(\mathbf{X}_{i,k} - \hat{\mathbf{x}}_{k|k-1} \right) \left(\mathbf{X}_{i,k} - \hat{\mathbf{x}}_{k|k-1} \right)^{\mathrm{T}} + \mathbf{Q}_k \tag{30}$$

Note, that these equations make use of the weight factors, Eqs. (25) through (27). Moreover, in Eq. (30), $\mathbf{Q}_k$ is the process noise covariance matrix.

With the prediction estimates $\hat{\mathbf{x}}_{k|k-1}$ and $\mathbf{P}_{k|k-1}$, a new set of $2L + 1$ sigma-points is calculated through the measurement function h:

$$\mathbf{z}_i = h(\boldsymbol{\chi}_{i,k}) \qquad \text{for } i = 0, ..., 2L \tag{31}$$

American Institute of Aeronautics and Astronautics

with which the empirical mean and covariance of the transformed points are calculated:

$$\hat{\mathbf{z}} = \sum_{i=0}^{2L} W_i^m \mathbf{z}_i \tag{32}$$

$$\mathbf{E}_{s,k} = \sum_{i=0}^{2L} W_i^c \left(\mathbf{z}_i - \hat{\mathbf{z}} \right) \left(\mathbf{z}_i - \hat{\mathbf{z}} \right)^{\mathrm{T}} + \mathbf{R}_k \tag{33}$$

with $\mathbf{R}_k$ being the covariance matrix of the observation noise, $\mathbf{w}_k$.

An estimate of the cross covariance matrix can be calculated from these obtained results:

$$\mathbf{C}_{xz} = \sum_{i=0}^{2L} W_i^c \left(\mathbf{X}_{i,k} - \hat{\mathbf{x}}_{k|k-1} \right) \left(\mathbf{z}_i - \hat{\mathbf{z}} \right)^{\mathrm{T}} \tag{34}$$

The Kalman gain is then

$$\mathbf{K}_k = \mathbf{C}_{xz} \mathbf{E}_{s,k}^{-1} \tag{35}$$

and, finally, the updated mean and covariance estimates are

$$\hat{\mathbf{x}}_{k|k} = \hat{\mathbf{x}}_{k|k-1} + \mathbf{K}_k (\mathbf{z}_k - \hat{\mathbf{z}}) \tag{36}$$

$$\mathbf{P}_{k|k} = \mathbf{P}_{k|k-1} - \mathbf{K}_k \mathbf{E}_{s,k} \mathbf{K}_k^{\mathrm{T}} \tag{37}$$

References

[1] Razgus, B., Mooij, E. and Choukroun, D., "Relative Navigation in Asteroid Missions Using Dual Quaternion Filtering", *Journal of Guidance, Control, and Dynamics*, Vol. 40, No. 9, pp. 2151–2166, 2017.

[2] Antreasian, P.G., Chesley, S.R., Miller, J.K., Bordi, J.J., and Williams, B.G., "The design and navigation of the near Shoemaker landing on Eros", AAS-01-372, *Advances in the Astronautical Sciences*, Vol. 109 II, 2002.

[3] Miller, J.K., Konopliv, A.S., Antreasian, P.G., Bordi, J.J., Chesley, S., Helfrich, C.E., Owen, W.M., Wang, T.C., Williams, B.G., Yeomans, D.K., and Scheeres, D.J., "Determination of shape, gravity, and rotational state of asteroid 433 Eros", *Icarus*, Vol. 155, No. 1, pp. 3–17 , 2002.

[4] Vallado, D.A., *Fundamentals of Astrodynamics and Applications*, McGraw-Hill, Inc., New York, NY, 2001.

[5] Root, B.C., Novák, P., Dirkx, D., Kaban, M.K., Van der Wal, W., and Vermeersen, L.L.A., "On a spectral method for forward gravity field modelling", *Journal of Geodynamics*, Vol. 97, pp. 22–30, 2016.

[6] Wan, E.A., and Van Der Merwe R., "The Unscented Kalman Filter for Nonlinear Estimation", *Adaptive Systems for Signal Processing, Communications, and Control Symposium*, pp.153–158, 2000.

[7] Farrell, J.A. and Barth, M., *The Global Positioning System & Inertial Navigation*, McGraw-Hill, New York, 1999.

[8] Welch, G. and Bishop, G., "An Introduction to the Kalman Filter", SIGGRAPH 2001 Course 8, University of North Carolina at Chapel Hill, 2001.

[9] Groves, P.D., *Principles of GNSS, Inertial, and Multisensor Integrated Navigation Systems*, Artech House, 2008.

[10] Julier, S. and Uhlmann, J., "Unscented Filtering and Nonlinear Estimation", *Proceedings of the IEEE*, Vol. 92, Nr. 3, pp. 401-422, 2004.